ELSEVIER

Volume 185, January 2012

CONTENTS

JOURNAL OF SOLID STATE CHEMISTRY

www.elsevier.com/locate/jssc

Abstracted/indexed in BioEngineering Abstracts, Chemical Abstracts, Coal Abstracts, Current Contents/Physics, Chemical, & Earth Sciences, Engineering Index, Research Alert, SCISEARCH, Science Abstracts, and Science Citation Index. Also covered in the abstract and citation database SciVerse SCOPUS®. Full text available on SciVerse ScienceDirect®.

Regular Articles

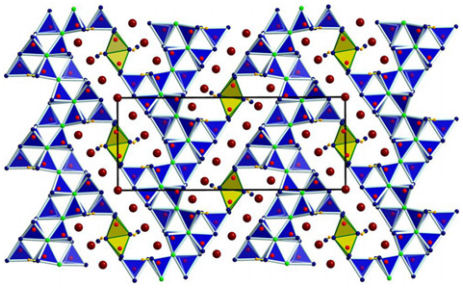

The new high-pressure borate hydrate $Co_7B_{24}O_{42}(OH)_2 \cdot 2\,H_2O$ is built up from corner-sharing BO_4 tetrahedra forming corrugated layers, that are interconnected among each other by two edge-sharing BO_4 tetrahedra (B_2O_6 units). In this paper we report on synthesis, structural details, and properties of the new compound $Co_7B_{24}O_{42}(OH)_2 \cdot 2\,H_2O$.

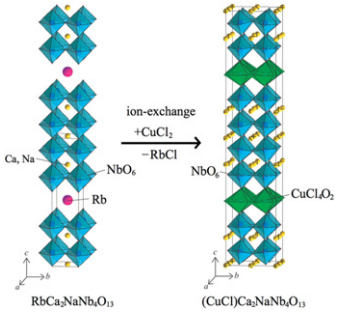

We present a quadruple-layered copper oxyhalide $(CuCl)Ca_2NaNb_4O_{13}$ synthesized through a topotactic ion-exchange reaction of $RbCa_2NaNb_4O_{13}$ with $CuCl_2$. The compound has a well-defined superstructure. Magnetic studies suggest the absence of magnetic order even at 2 K.

Regular Articles

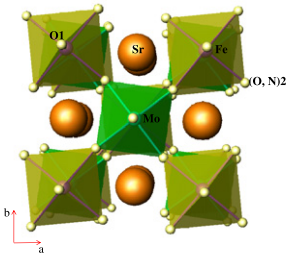

We have synthesized and studied the new oxinitride double perovskites $Sr_2FeMoO_{6-x}N_x$. They present anionic ordering between O and N. The nitridation process improves the long-range Fe/Mo ordering. They show a ferrimagnetic transition with a reduced saturation magnetization compared to Sr_2FeMoO_6, due to the different nature of the double exchange interactions through Fe–N–Mo–N–Fe in contrast to Fe–O–Mo–O–Fe. We suggest a shift towards a configuration $Fe^{4+}(3d^4, S=2)$:$Mo^{5+}(4d^1, S=1/2)$.

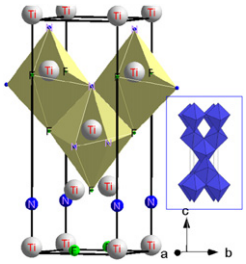

The geometry optimized ground state anatase derived TiNF structure with arrangement of open faceted *TiN3F3* distorted octahedra. The insert shows the arrangement of octahedra in anatase TiO_2.

Continued

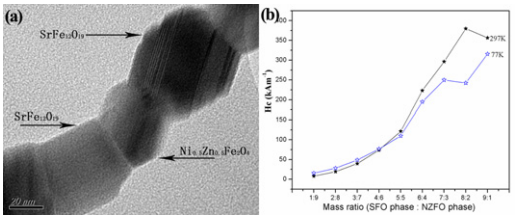

$SrFe_{12}O_{19}$ (SFO)/$Ni_{0.5}Zn_{0.5}Fe_2O_4$ (NZFO) composite ferrite nanofibers with a uniform phase distribution show competition of the exchange–coupling interaction and the dipolar interaction in the composite nanofibers.

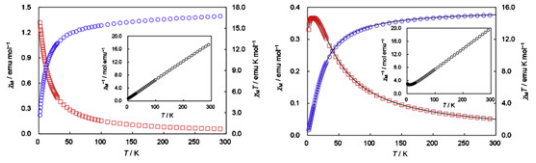

Three-dimensional porous and two-dimensional layered manganese isophthalates have been prepared. Magnetic susceptibility measurements exhibit overall weak antiferromagnetic interactions between the Mn(II) ions in both compounds.

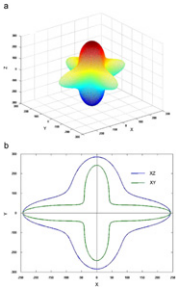

(a) Directional dependence of Young's modulus in zircon-type YVO_4 and (b) projections of the directional dependent Young's modulus in different planes for zircon-type YVO_4. The units are in GPa.

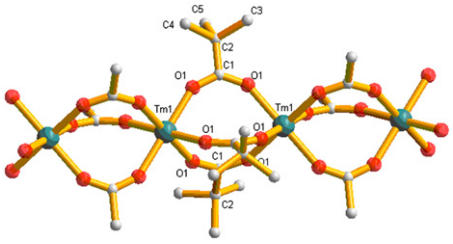

Novel 1D coordination polymer $\{Tm(Piv)_3\}_n$ was synthesized and studied by X-ray diffraction. The magnetic, luminescence properties, the thermal behavior and the volatility for the compound $\{Tm(Piv)_3\}_n$ were investigated.

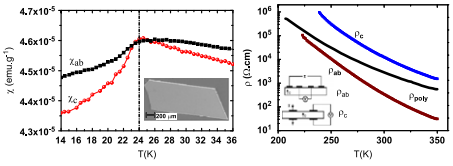

3R-$CuCrO_2$ platelet-like single crystals have been successfully grown by the flux method. As revealed by $\chi(T)$ and $C(T)$ measurements, their properties are characterised by a unique antiferromagnetic transition at $T_N = 24$ K. Interestingly, despite a very small magnetic anisotropy, a large one is evidenced by the resistivity ratio, $\rho_c/\rho_{ab} \sim 35$, at 300 K. This suggests an easier charge hopping in the $[CrO_2]$ planes rather than along (Cr–O–Cu) pathways, i.e. along c axis.

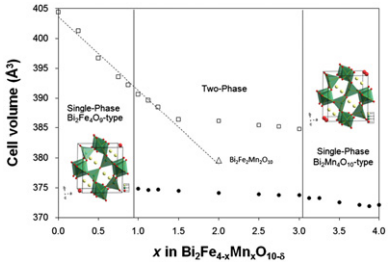

Single-phase regions are found near each end-member and a two-phase region is observed at intermediate compositions, extending from about $x = 1$ to 3, according to the general formula of the mixed crystals $Bi_2Fe_{4-x}Mn_xO_{10-\delta}$.

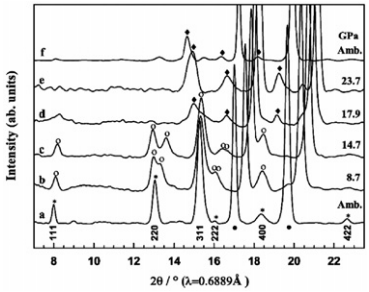

A series of phase transition of Fe_2TiO_4 occurs from cubic (a) to tetragonal (b and c) then to orthorhombic phase (d–f) at high pressure.

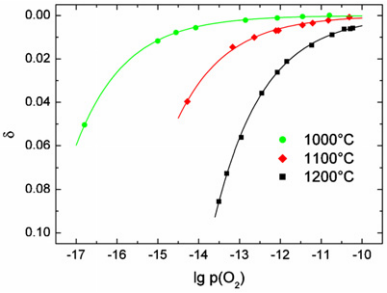

Nonstoichiometry δ of $Sr_2FeMoO_{6-\delta}$ as function of oxygen partial pressure at 1000, 1100, and 1200 °C.

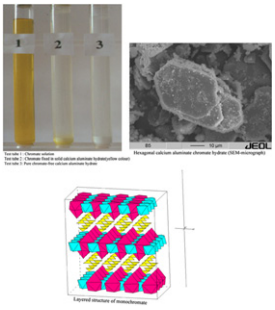

Chromate can be incorporated in LDH-phases with compositions like: $3CaO \cdot Al_2O_3 \cdot 1/2CaCrO_4 \cdot 1/2Ca(OH)_2 \cdot nH_2O$, $3CaO \cdot Al_2O_3 \cdot CaCrO_4 \cdot nH_2O$, $3CaO \cdot Al_2O_3 \cdot 1/6CaCrO_4 \cdot 5/6Ca(OH)_2 \cdot nH_2O$, $3CaO \cdot Al_2O_3(0-x)CaCrO_4(1-x)\ Ca(OH)_2 \cdot 12H_2O$, $(0<x<0.17)$.

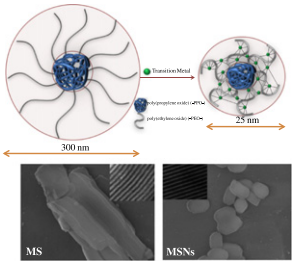

Metal-chelating surfactant micelle templates support a simple and facile preparations of size-tunable ordered MSNs.

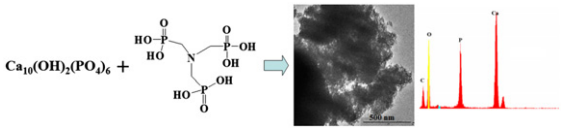

Hydroxyapatite in the form of naturally occurring phosphate rock is converted in the presence of nitrilotris(methylene)triphosphonate (NTP) to high surface area apatite nanoparticles (dimensions measured by TEM) with NTP-functionalized surfaces.

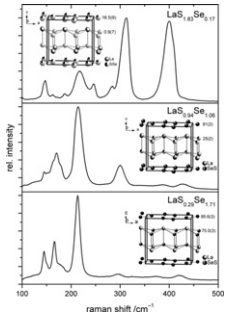

Raman spectra and site occupancies in the structures of selected lanthanum sulfide selenides.

Continued

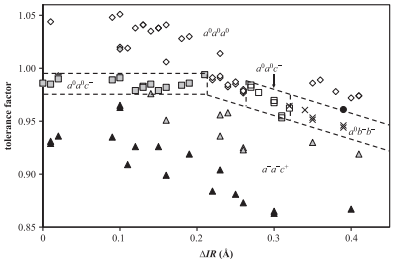

A survey of the tolerance factor of 41 Mo/W- and 52 Nb/Ta-containing quaternary perovskites plotted as a function of the difference between the two six-coordinate *M*-cation ionic radii. Compounds with cubic symmetry are represented by diamonds, those with tetragonal symmetry are represented by squares, those with *I*2/*m* monoclinic symmetry are represented by ×, and those with $P2_1/n$ monoclinic symmetry are represented by triangles. White symbols represent compositions where $A = Ba^{2+}$, gray symbols represent compositions where $A = Sr^{2+}$, and black symbols represent where $A = Ca^{2+}$. The filled circle represents rhombohedral Ba_2BiTaO_6 ($t = 0.961$; space group—*R*3?; tilt system—$a^-a^-a^-$). References for the compounds included in this figure are listed in the Supporting Information File.

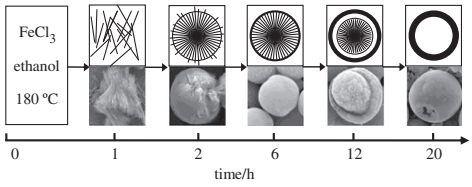

Fe_2O_3 homogeneous core/shell hierarchical microspheres were synthesized by solvothermal method. Owing to the special structure, the synthesized Fe_2O_3 microspheres exhibit a superior catalytic activity in benzyl oxidation.

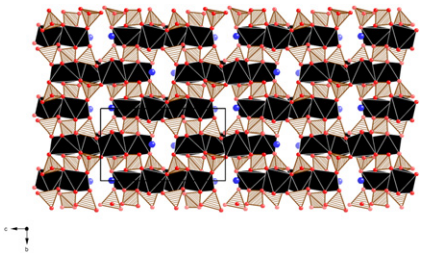

Stacking of the layers in $CsU_2(PO_4)_3$, viewed along [100].

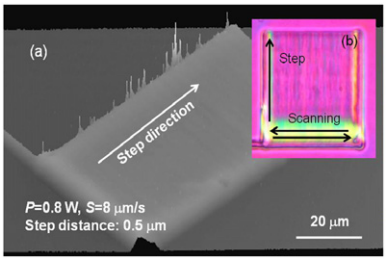

This figure shows confocal scanning laser microscope and polarized optical microscope photographs for β-BaB_2O_4 crystals obtained by laser irradiations. The laser scanning was repeated with a step of 0.5 μm between the lines using the condition of the power of $P = 0.8$ W and a laser scanning speed of $S = 8$ μm/s. It is suggested that β-BaB_2O_4 crystals in the overlapped laser-irradiated region are highly oriented and the *c*-axis direction of β-BaB_2O_4 crystals is perpendicular to the laser scanning direction.

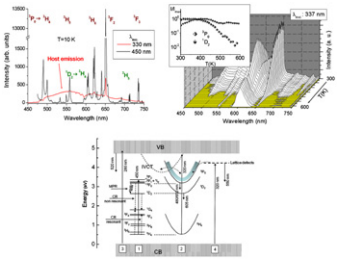

A general scheme is proposed in order to account for the complex dependence of the luminescence properties of the $CaMoO_4:Pr^{3+}$ system on the experimental parameters including excitation wavelength, temperature, doping concentration, etc.

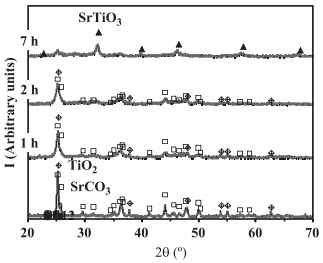

X-Ray diffractograms of the starting TiO_2 (anatase) + $SrCO_3$ mixture and after mechanical activation at 650 rpm, for 1, 2, and 7 h. Different symbols are used to identify reflections ascribed to anatase (diamonds), $SrCO_3$ (squares) and $SrTiO_3$ (triangles).

Intercalation studies of zinc hydroxide chloride: Ammonia and amino acids
Gregorio Guadalupe Carbajal Arízaga
page 150

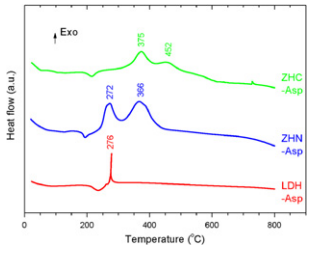

The zinc hydroxide chloride (ZHC) with formula $Zn_5(OH)_8Cl_2 \cdot 2H_2O$ was tested as intercalation matrix. In comparison with the well-known zinc hydroxide nitrate (ZHN) and layered double hydroxides (LDH), ZHC was the best matrix for thermal protection of Asp combustion, presenting exothermic peaks even at 452 °C, while the highest exothermic event in ZHN was at 366 °C, and in the LDH it was at 276 °C.

The hunt for LaFeSbO: Synthesis of La_2SbO_2 and a case of mistaken identity
Sean Muir, Jason Vielma, Guenter Schneider, A.W. Sleight and M.A. Subramanian
page 156

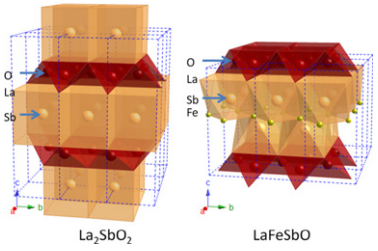

The layered oxypnictide compounds La_2SbO_2 and $La_{1.9}Sr_{0.1}SbO_2$ have been synthesized and investigated. Both crystallize in a $ThCr_2Si_2$ type configuration and are semiconducting. Stability of the unreported compound LaFeSbO has been investigated using density functional theory. A case of mistaken identity in the literature regarding the composition LaNiBiO is addressed.

Investigation of the iron site localization in doped ZnO
M.D. Carvalho, L.P. Ferreira, R.P. Borges and M. Godinho
page 160

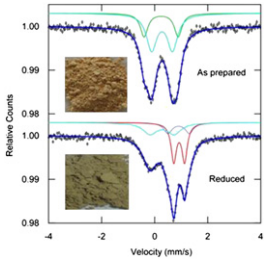

$Zn_{0.95}Fe_{0.05}O$ obtained by a combustion method and after reduction under hydrogen atmosphere.

The synthesis, structure, magnetic and luminescent properties of a new tetranuclear dysprosium (III) cluster
Yen-Han Chen, Yun-Fan Tsai, Gene-Hsian Lee and En-Che Yang
page 166

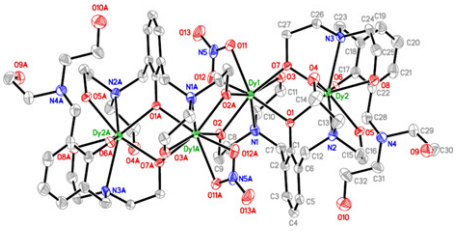

A new tetranuclear dysprosium (III) complex $[Dy_4(dhampH_3)_4(NO_3)_2](NO_3)_2$ is synthesized and reported in this paper. This molecule has luminescence and can potentially act as a SMM.

Controlled synthesis of $MnSn(OH)_6$/graphene nanocomposites and their electrochemical properties as capacitive materials
Gongkai Wang, Xiang Sun, Fengyuan Lu, Qingkai Yu, Changsheng Liu and Jie Lian
page 172

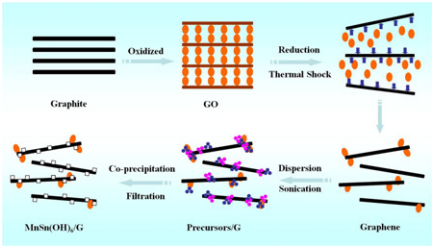

Graphite oxide (GO) can be synthesized by oxidizing graphite using Hummers method. Graphene was reduced from GO by thermal exfoliation. In this work, $MnSn(OH)_6$/graphene nanocomposites were synthesized by a simple co-precipitation method and their electrochemical performances have been explored.

$[La(UO_2)V_2O_7][(UO_2)(VO_4)]$ the first lanthanum uranyl-vanadate with structure built from two types of sheets based upon the uranophane anion-topology
A. Mer, S. Obbade, M. Rivenet, C. Renard and F. Abraham
page 180

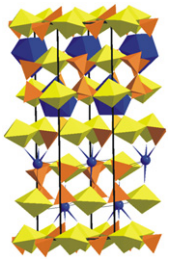

A view of the three-dimensional structure of $[La(UO_2)V_2O_7][(UO_2)(VO_4)]$.

Continued

Photoluminescence properties of rare earths (Eu^{3+}, Tb^{3+}, Dy^{3+} and Tm^{3+}) activated $NaInW_2O_8$ wolframite host lattice

S. Asiri Naidu, S. Boudin, U.V. Varadaraju and B. Raveau

page 187

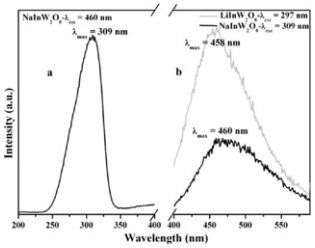

$NaInW_2O_8$ double tungstate doped with Eu^{3+}, Dy^{3+}, Tb^{3+} and Tm^{3+} shows characteristic emission of intense red for Eu^{3+}, yellow for Dy^{3+}, green for Tb^{3+} and blue for Tm^{3+}.

Synthesis and characterization of a nanocomposite of goethite nanorods and reduced graphene oxide for electrochemical capacitors

Qingliang Shou, Jipeng Cheng, Li Zhang, Bradley J. Nelson and Xiaobin Zhang

page 191

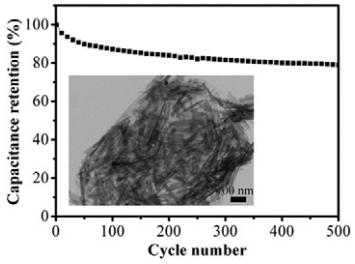

The reduced graphene oxide sheets are decorated with goethite nanorods. The as-prepared composite exhibits a high electrochemical capacitance with good recycling capability, which is promising for supercapacitor applications.

Synthesis of Co-containing mesoporous carbon foams using a new cobalt-oxo cluster as a precursor

Yao-Kang Lv, Yun-Long Feng, Li-Hua Gan, Ming-Xian Liu, Liang Xu, Cao Liu, Hao-Wen Zheng and Jie Li

page 198

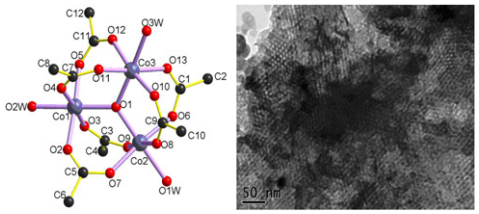

A new trinuclear cobalt-oxo cluster, $2[Co_3O(Ac)_6(H_2O)_3]\cdot H_2O$ (**1**), was obtained and further used as a precursor to synthesize Co-containing mesoporous carbon foams (Co-MCFs) which exhibit improved electrochemical behaviors.

Structural, energetic and thermodynamic analyses of $Ca(BH_4)_2\cdot 2NH_3$ from first principles calculations

Peng-Fei Yuan, Fei Wang, Qiang Sun, Yu Jia and Zheng-Xiao Guo

page 206

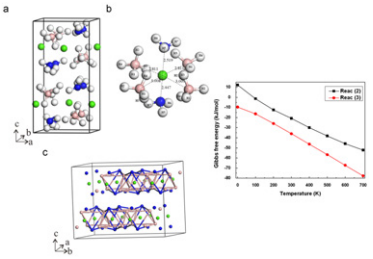

The crystal structure of this compound and the calculated decomposition reaction free energy for two different reactions:

$$\text{Reac (2)}: Ca(BH_4)_2\cdot 2NH_3 \overset{162^{\circ}C}{\rightarrow} Ca(BH_4)_2\cdot NH_3 + NH_3 \overset{230^{\circ}C}{\rightarrow} Ca(BH_4)_2 + 2NH_3$$

$$\text{Reac (3)}: Ca(BH_4)_2\cdot 2NH_3 \overset{190^{\circ}C}{\rightarrow} 1/4Ca(BH_4)_2 + 1/4Ca_3(BN_2)_2 + BN + 6H_2$$

Structural studies of magnesium nitride fluorides by powder neutron diffraction

Michael A. Brogan, Robert W. Hughes, Ronald I. Smith and Duncan H. Gregory

page 213

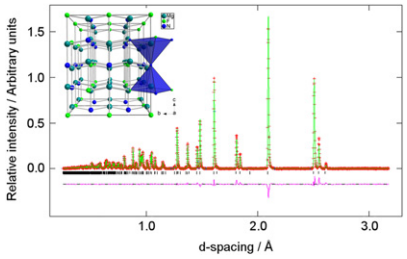

Definitive structures of the ternary magnesium nitride fluorides Mg_3NF_3 and the lower temperature polymorph of Mg_2NF have been determined from powder neutron diffraction data. The nitride halides are essentially ionic and exhibit weak temperature independent paramagnetic behaviour.

8-Hydroxypyrene-1,3,6-trisulphonate and octanesulphonate co-assembled layered double hydroxide and its controllable solid-state luminescence by hydrothermal synthesis

Sile Dang, Dongpeng Yan and Jun Lu

page 219

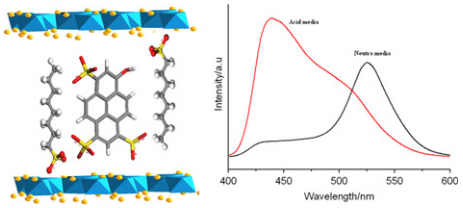

8-Hydroxy-pyrene-1,3,6-trisulphonate and octanesulfonate co-intercalated ZnAl layered double hydroxide can exhibit tunable solid-state blue and green fluorescence by treating the sample at acid and neutral media under hydrothermal condition.

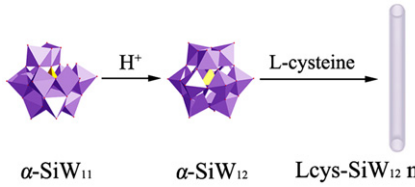

The Lcys-SiW_{12} microtubes were formed during transformation of the monolacunary Keggin-type $[\alpha\text{-}SiW_{11}O_{39}]^{8-}$ to the saturated Keggin-type $[\alpha\text{-}SiW_{12}O_{40}]^{4-}$, meanwhile L-cysteine molecules were doped during the growth of the microtubes.

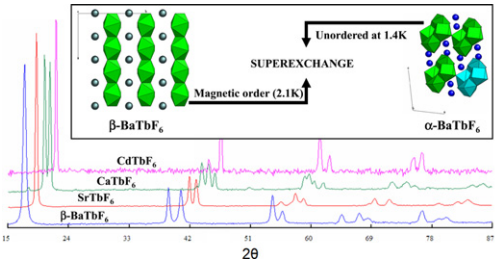

Powder neutron diffraction revealed magnetic order in four of the five investigated fluoroterbates, while crystal chemical analyses of α and β forms of $BaTbF_6$ evidenced the existence of superexchange interactions.

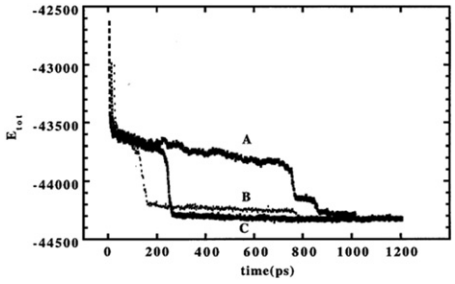

Time dependence of energy per atom in the quenching of liquid nanoparticles A–C of iron. Nanoparticle C freezes directly into a single crystal but A and B freeze to solids with two grains. A and B eventually recrystallize into single crystals.

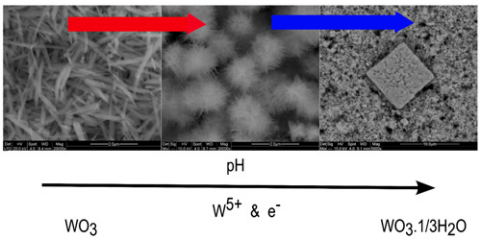

The figure illustrates the role of pH in morphological and absorption edge evolution of WO_3 (hydrate) as well as the variation in the concentration of defect electrons between anhydrous and hydrated WO_3.

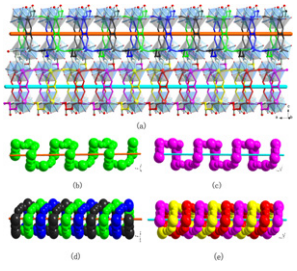

$[R_2(tar)_2(C_2O_4)(H_2O)_2]_n \cdot 4nH_2O$ (R = La (**2**), Nd (**3**)) display rare **fsx**-4,5-$P2_1/c$ topology containing hydrophilic channels bounded by triple helical chains along a axis.

Rapid Communication

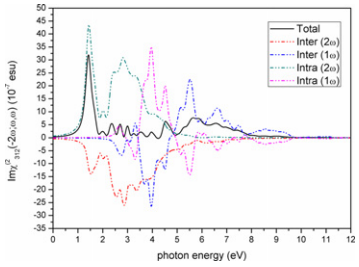

Calculated total imaginary part of $\chi^{(2)}_{312}(-2\omega;\omega,\omega)$ spectra along with the intra-(2ω)/(1ω) and inter-(2ω)/(1ω) band contributions.

Continued